


Impact of confinement and polarizability on dynamics of ionic liquids ^F

Cite as: J. Chem. Phys. **156**, 064703 (2022); <https://doi.org/10.1063/5.0077408>

Submitted: 02 November 2021 • Accepted: 07 January 2022 • Accepted Manuscript Online: 21 January 2022 • Published Online: 08 February 2022

 Johannes Gäding,  Gabriele Tocci,  Mark Busch, et al.

COLLECTIONS

 This paper was selected as Featured



View Online



Export Citation



CrossMark

ARTICLES YOU MAY BE INTERESTED IN

Chemical physics software

The Journal of Chemical Physics **155**, 010401 (2021); <https://doi.org/10.1063/5.0059886>

Phase diagram of the NaCl-water system from computer simulations

The Journal of Chemical Physics **156**, 064505 (2022); <https://doi.org/10.1063/5.0083371>

Constant potential simulations on a mesh

The Journal of Chemical Physics **155**, 104104 (2021); <https://doi.org/10.1063/5.0063381>

Lock-in Amplifiers
up to 600 MHz



Zurich
Instruments



Impact of confinement and polarizability on dynamics of ionic liquids

Cite as: J. Chem. Phys. 156, 064703 (2022); doi: 10.1063/5.0077408

Submitted: 2 November 2021 • Accepted: 7 January 2022 •

Published Online: 8 February 2022



Johannes Gäding,¹  Gabriele Tocci,²  Mark Busch,^{3,4,5}  Patrick Huber,^{3,4,5} 
and Robert H. Meißner^{1,6,a)} 

AFFILIATIONS

¹Institute of Polymers and Composites, Hamburg University of Technology, 21073 Hamburg, Germany

²Department of Chemistry, University of Zurich, 8057 Zürich, Switzerland

³Institute for Materials and X-Ray Physics, Hamburg University of Technology, 21073 Hamburg, Germany

⁴Deutsches Elektronen-Synchrotron DESY, Centre for X-Ray and Nano Science CXNS, 22607 Hamburg, Germany

⁵Centre for Hybrid Nanostructures CHyN, Hamburg University, 22761 Hamburg, Germany

⁶Helmholtz-Zentrum Hereon, Institute of Surface Science, 21502 Geesthacht, Germany

^{a)}Author to whom correspondence should be addressed: robert.meissner@tuhh.de

ABSTRACT

Polarizability is a key factor when it comes to an accurate description of different ionic systems. The general importance of including polarizability into molecular dynamics simulations was shown in various recent studies for a wide range of materials, ranging from proteins to water to complex ionic liquids and for solid–liquid interfaces. While most previous studies focused on bulk properties or static structure factors, this study investigates in more detail the importance of polarizable surfaces on the dynamics of a confined ionic liquid in graphitic slit pores, as evident in modern electrochemical capacitors or in catalytic processes. A recently developed polarizable force field using Drude oscillators is modified in order to describe a particular room temperature ionic liquid accurately and in agreement with recently published experimental results. Using the modified parameters, various confinements are investigated and differences between non-polarizable and polarizable surfaces are discussed. Upon introduction of surface polarizability, changes in the dipole orientation and in the density distribution of the anions and cations at the interface are observed and are also accompanied with a dramatic increase in the molecular diffusivity in the contact layer. Our results thus clearly underline the importance of considering not only the polarizability of the ionic liquid but also that of the surface.

© 2022 Author(s). All article content, except where otherwise noted, is licensed under a Creative Commons Attribution (CC BY) license (<http://creativecommons.org/licenses/by/4.0/>). <https://doi.org/10.1063/5.0077408>

I. INTRODUCTION

Room temperature ionic liquids (RTILs) are considered as promising materials for a wide range of chemical and electrical applications. The growing attention to these materials rises mainly from their distinct properties: As a room temperature molten salt, they have almost no vapor pressure, a high thermal stability, and a large liquidus and electrochemical window.^{1–5} Ionic liquids are used as solvents in the processing of aerogels, as a silica supported catalyst in water and in other homogeneous and heterogeneous catalytic processes.^{6–12} Concerning electrochemistry, they attract great attention as promising electrolytes in energy storage applications such as batteries and supercapacitors^{13–16} and their associated charging dynamics have been extensively studied with molecular

simulations.^{17–19} However, the conductivity of ionic liquids is generally rather low²⁰ and can be increased by the addition of solvents that effectively reduce their viscosity.^{21,22} With the ever increasing emergence of nanoporous carbons as electrodes or as support materials for catalytic reactions in combination with RTILs, the interactions between those materials and the resulting dynamics are of great interest as RTILs often continue to exceed expectations, for example, in terms of high voltage charging^{15,23} and increasing catalytic effectiveness.^{24,25}

Several molecular dynamics studies have been conducted previously employing a broad range of different force fields to obtain fundamental insights into the structure and dynamics of ionic liquids in contact with carbonaceous structures.^{26–31} While most force

fields with fixed atomic partial point charges are able to reproduce structural data from experiments, they typically underestimate the dynamical properties of RTILs by orders of magnitude.^{32–34} In particular, ion-dynamics are important for modeling and optimizing the charging and discharging processes in carbon based supercapacitors, for instance.³⁵ A commonly used work-around to reproduce effectively correct dynamics of the RTILs is to scale down some of their atomic point charges. However, this scaling leads to inaccuracies in the description of the dielectric and structural properties and often yields incorrect densities.^{36,37} Ionic liquids are rather large ionic molecules with mostly strongly delocalized charges. Their often polar aromatic side groups are thus exposed to pronounced electrostatic forces. A straightforward approach to improve the representation of electrostatics, and hence dynamic properties, is the explicit modeling of the polarization.^{34,38–41} In addition, several works in the past have proven that a polarizable treatment of the surfaces, especially when in contact with RTILs, plays a key role.^{42–45} However, previous studies have focused either on other material combinations (e.g., water–graphene or saline–gold) or merely structural properties of RTILs.

In this work, we illustrate that the surface and liquid polarizabilities play a crucial role in determining the dynamics of ionic liquids at electrode interfaces. A polarizable semi-empirical Drude–Lennard-Jones force field is adjusted to accurately describe the ionic liquid 1-butylpyridinium bis(trifluoromethane) sulfonimide [BuPy][NTf₂]. The modified parameter set is validated against experimental data in terms of dynamical and structural properties in the bulk phase.^{46,70} After validation, different slit-pore confinements (cf. Fig. 1) are investigated in order to obtain a detailed insight in the behavior of the RTILs at the solid–liquid interface on an atomic scale. Finally, the focus of this work lies on the investigation of the influence of a polarizable surface on the dynamical properties, e.g., diffusion coefficients—with a remarkable enhancement of near-surface diffusion—and the associated structural ordering of an RTIL in confinement.

II. METHODS

All simulations are performed within the framework of molecular dynamics using the Large-scale Atomic/Molecular Massively

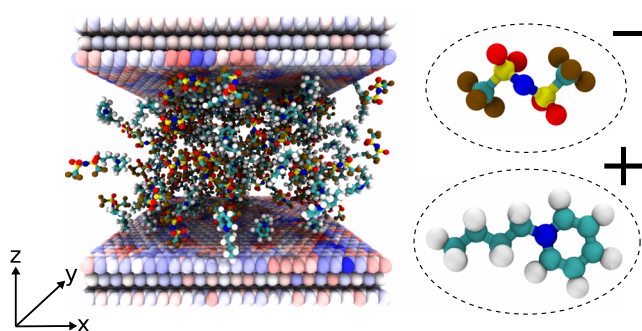


FIG. 1. Snapshot of the 4.09 nm slit-pore confinement. For visualization, 33% of the RTIL [BuPy][NTf₂] are shown along with the dipole orientation normal to the surface in the graphite layers (positive charge toward the RTIL: red; positive charge toward the RTIL: blue). The color coding of the RTIL atoms is as follows: N: blue, C: teal, O: red, S: yellow, F: brown, and H: white.

Parallel Simulator (LAMMPS).⁴⁷ LAMMPS was built with the USER-DRUDE package to enable the polarization of atoms by Drude oscillators.⁴⁸ The resulting data are visualized using Visual Molecular Dynamics (VMD).⁴⁹ VMD is also used to create initial slit pores with graphene layers of different sizes. Initial configurations of the ionic liquid are generated using the fftool⁵⁰ that relies on PACKMOL.⁵¹

Short-range van der Waals interactions are described by a 12-6 Lennard-Jones (LJ) potential and use the same 12 Å cutoff as the real-space Coulomb interactions. In addition, long-range electrostatic interactions are computed with a particle–particle particle-mesh (PPPM) solver. Parameters for an unpolarized ionic liquid [BuPy][NTf₂] are taken from the CL & P force field.⁵² The recently released CL & Pol force field was employed to take polarizabilities into account by employing Drude oscillators.^{40,53,54} Short-ranged electrostatic interactions between induced dipoles are effectively reduced by Thole functions preventing excessive correlations between neighboring Drude particles.⁵⁵ The integration of Drude particles into the CL & P force field is accomplished according to the method of Lamoureux and Roux.⁴⁸ Atomic polarizabilities of the ionic liquid are modeled by introducing additional Drude particles on heavy atoms as proposed by Goloviznina *et al.*⁴⁰ and Schröder.⁵⁶ All calculations related to confined states employ the CP & Pol polarizable force field for the description of the ionic liquid.

To account for image charge effects, graphite is polarized in a procedure similar to that used previously for gold⁵⁷ using a method described in the work of Geada *et al.*⁴⁴ which allows us to describe electrode polarization in a consistent way without requiring too much additional computational effort. Alternatively, a fixed potential approach^{58–60} or an electrostatic layer correction with image charges (ELCIC)⁶¹ could be utilized. For graphite atoms, a per-atom polarizability of 0.867 Å³ is used as obtained from *ab initio* calculations of the out-of-plane polarization of few layer graphenes in a vacuum.⁶² Ho and Striolo⁴² investigated the impact of surface polarization of trilayer graphene in contact with water using a comparable value for the per-atom-polarizability. Misra and Blankschtein⁶³ employed a somewhat larger value of 1.139 Å³ in their studies of the water/graphene interface in order to take the anisotropic character of the polarization into account. Although anisotropic Drude oscillators would generally be preferable, in this study, we chose the polarizability of Yu *et al.*⁶² to avoid overestimating the out-of-plane polarization, as an anisotropic polarization of electrode atoms is not yet possible with current simulation approaches. Aside from the scaling of the intermolecular energy-related variable ϵ in the LJ potential (according to the symmetry-adapted perturbation theory values of Goloviznina *et al.*⁴⁰), a reasonable σ parameter scaling is obtained by evaluating various scaling factors besides the suggested one of 0.985.⁴⁰ The obtained simulation results are compared to experiments of Busch *et al.*,⁴⁶ which considered the bulk density and self-diffusion coefficient of the cation.

All calculations are performed with a time step of 0.25 fs and contained 300 ion pairs of the RTIL to ensure accurate calculations of the mean square displacement.⁴⁰ This rather small time step ensured stable simulations and accurate dynamics despite the small mass of the additional Drude oscillators. Bulk phase calculations with periodic boundary conditions in all three dimensions are used for equilibration using a NPT ensemble employing a Nosé–Hover barostat and thermostat at 340 K and 1 atm pressure. In contrast,

slit-pore walls restrict the RTIL in the z -dimension, and hence, a 2D k -space modification is used.⁶⁴ Pore walls are modeled by a stack of three graphene layers on each side of the RTIL. According to previous studies, three layers have been proven sufficient to model a polarizable surface.^{42,44,65} To ensure atmospheric conditions, slit pores were exposed to a force equal to a pressure of 1 atm applied to the upmost three layers that act thus as a piston on the whole system. The pressure was held constant until the pore walls reached their equilibrium positions in which they were then fixated. To keep the computations feasible, different pore heights are created by varying the surface area of the slit pores while keeping the amount of ionic liquid constant. As a result, slit pores with a distance between the walls of 4.09, 2.36, and 1.65 nm are generated. Besides the usage of (modified) CL & P force field parameters for the ionic liquid, parameters for electrode carbons are taken from the OPLS-AA force field.⁶⁶ LJ interactions between different species are calculated according to the required geometrical mixing rules of OPLS-AA.⁶⁷

The slow dynamics of the ionic liquid required a specific equilibration using different temperatures (cf. [supplementary material](#), Sec. I B). A detailed description of the force field parameters as well as the simulation setup is given in the [supplementary material](#).

A. Mean square displacement

The mean squared displacement (MSD) of a particular atomic species can be calculated according to

$$\langle r^2(\tau) \rangle = \frac{1}{N} \cdot \sum_{i=1}^N (\vec{r}_i(t + \tau) - \vec{r}_i(t))^2. \quad (1)$$

Therein, the displacement r within a certain period of time τ of each particle i of a given species is averaged. Equivalently, a MSD of an individual spatial dimension can be obtained by using one coordinate component, e.g. x , in the calculation. Each production run for calculating the MSD in the whole pore lasts 10 ns, which is considered to be sufficient according to other works.⁴⁰

The diffusion coefficient is obtained from the slope of the MSD by employing the Einstein relation, with n being the number of considered spatial dimensions. While all three dimensions ($n = 3$) were considered for the bulk calculations, only the displacements in x - and y -dimensions are considered for the confined state ($n = 2$) since diffusion is restricted in the z -direction. As the displacement in each spatial dimension is independent from other dimensions, the two-dimensional diffusion coefficient D_{xy} is given by

$$D_{xy} = \frac{1}{2n} \lim_{\tau \rightarrow \infty} \frac{d}{d\tau} \cdot (\langle r_x^2(\tau) \rangle + \langle r_y^2(\tau) \rangle). \quad (2)$$

To investigate the influence of polarizable surfaces on the dynamics of the confined ionic liquid, especially in the contact layer, trajectories of individual molecules are partitioned as described below to calculate specific diffusion coefficients within molecular layers. Each layer height is defined by two minima in the density profiles as illustrated in [Fig. 4](#). Since the differences in the overall density profile of the ionic liquids for polarizable and non-polarizable surfaces are marginal, the same layering was used in both cases. In order to avoid highly fragmented trajectories, layer transitions are triggered if a molecule moves across a layer boundary for more than 25 ps.

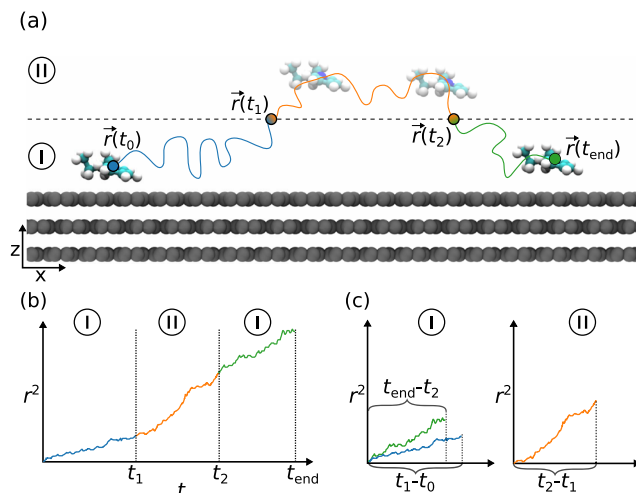


FIG. 2. Schematic representation of the method used to calculate the mean square displacement layer-wise by partitioning trajectories. (a) Molecule i diffuses in the pore within total simulation time $\tau_{\text{tot}} = t_{\text{end}} - t_0$. During the simulation, two layer transitions take place on time steps t_1 and t_2 , respectively. (b) The displacement is partitioned according to these two layer transitions. (c) Resulting per-layer displacements of the traced molecule.

[Figure 2](#) illustrates exemplarily the approach to partition a trajectory for the case of a twofold layer transition. During the entire movement, two layer transitions occur, the first at time step t_1 , when the particle moves from layer I to layer II, and the reverse transition from layer II to layer I at time step t_2 [cf. [Fig. 2\(a\)](#)]. Based on these two time steps, the trajectory is now partitioned into layer-wise partitions, as shown in [Fig. 2\(b\)](#). A new displacement is calculated for each partition, using as the initial position the location where the molecule enters the respective layer. The position, at which the molecule crosses the layer boundaries, thus represents both the end of the current and the new origin for the following displacement calculation. For instance, the first partition (blue curves in [Fig. 2](#)) ranges from the start of the overall simulation trajectory at t_0 to the first layer transition at t_1 with the total time τ_0 . The displacement of the first partition $\vec{r}_i(\tau_0)$ is calculated continuously starting from the origin at $\vec{r}_i(t_0)$ up to $\vec{r}_i(t_1)$,

$$\vec{r}_i(\tau_0) = \vec{r}_i(t_1) - \vec{r}_i(t_0). \quad (3)$$

Accordingly, the second partition covers the displacement that takes place in layer II after the first layer transition at $\vec{r}_i(t_1)$ and until the molecule leaves the layer at $\vec{r}_i(t_2)$ (orange curves in [Fig. 2](#)). The displacement of the following third partition is calculated from $\vec{r}_i(t_2)$ to the end of the overall simulation trajectory at $\vec{r}_i(t_{\text{end}})$ (green curves in [Fig. 2](#)). In the general case of K layer transitions, one obtains $K + 1$ individual trajectories by partitioning the trajectory of a specific molecule. Each of these partitions k covers only the timespan τ_k between its starting time step t_k , defined by the recent layer transition [or the simulation start for the first partition ($k = 0$)], and the last time step t_{k+1} , defined by the following layer transition [or the simulation end for the last partition ($k = K$)]:

$$\vec{r}_i(\tau_{\text{tot}}) = \sum_{k=0}^K (\vec{r}_i(t_{k+1}) - \vec{r}_i(t_k)). \quad (4)$$

According to these limits, the displacement $\vec{r}_i(\tau_k)$ by the continuously movement in one particular layer can be calculated,

$$\vec{r}_i(\tau_k) = \vec{r}_i(t_{k+1}) - \vec{r}_i(t_k). \quad (5)$$

The layer-wise partitions are treated as individual trajectories, which are used to calculate a mean square displacement for each particular layer, as shown in Fig. 2(c), by averaging over the ensemble. It should be noted that Fig. 2 shows artificial data and is only used to illustrate the approach to fragment the trajectory to estimate the MSD. The resulting data of our simulations can be found in Sec. II A of the [supplementary material](#). The resulting layer-wise trajectories have various lengths τ_k depending on the time a molecule remains in the respective layer continuously [cf. Fig. 2(c)]. This results in a decreasing number of trajectories with time and affects most critically layers with a low density. Diffusion constants are obtained from the slope of the layer-wise MSDs analogous to Eq. (2) and are calculated only up to the time step at which at least 20 individual layer-wise trajectories are available. The lower limit of the range used for the slope calculation is defined according to the transition to the ballistic regime, in which the MSD is no longer linear (i.e., 0.2 ns; see Fig. S4 of the [supplementary material](#)). The slope is weighted by the number of trajectories available at each specific point.

B. Induced dipoles

The induced dipole μ on the atoms is calculated from the displacement p of the specific Drude particle and its core atom in the presence of an electric field E arising from the fixed charges as well as all the other induced dipoles,

$$\mu = q_D \cdot p = \left(\frac{q_D^2}{k_D} \right) E, \quad (6)$$

where q_D is the charge on the Drude particle and k_D is the spring constant of the Drude bond.^{48,68} Dipoles induced by a single adsorbed ion on the substrate are estimated from a 2 ns gas phase production run without any other ionic liquid molecules at a temperature of 1.0 K (cf. Fig. S11 of the [supplementary material](#)). Since the system is not charge neutral in this specific case, an overall neutral system is ensured by introducing a neutralizing background charge.⁶⁹

III. RESULTS AND DISCUSSION

A. Bulk properties of the ionic liquid

Calculated bulk densities at 340 K for different σ -scaling factors Δ_σ are summarized in Table I. A scaling factor of 0.950 gives nearly perfect agreement with the experimentally determined bulk density as compared to the factor of 0.985 proposed by Goloviznina *et al.*⁴⁰ Consequently, this optimized value is used in all simulations where the polarizability of the RTIL is considered.

Including polarizabilities in the ionic liquid model enhances the diffusion of the cation by more than one magnitude as compared to an unpolarized description. After the scaling of σ with the optimized scaling factor, the diffusion enhances by another 25% and is in almost perfect agreement with previous experimental results. It should be noted here that correct scaling not only improves

TABLE I. Comparison of bulk densities of pure [BuPy][NTf2] at 340 K for different scalings Δ_σ of the Lennard-Jones σ parameter when Drude particles are introduced.

Δ_σ	ρ (g cm ⁻³)	D^+ (10 ⁻¹⁰ m ² s ⁻¹)	D^-
Unpol.	1.384	0.151	n/a
0.985	1.347	1.797	n/a
0.970	1.374	2.008	n/a
0.950	1.407	2.411	2.107
Exp. ⁷⁰	1.407	2.407	n/a

static quantities such as the bulk density; at the same time, it provides a correct estimate of dynamic quantities such as the diffusion coefficient.

B. Ionic liquid structure at the solid-liquid interface

The importance of an additional polarizable treatment of the pore surface atoms is investigated for three different nanosized slit pores. First, (symmetrical) density profiles of a confined RTIL in slit pores using polarizable or non-polarizable pore surfaces are compared in Figs. 3(a)–3(c). In general, only small differences in the total density profiles and electrostatic potentials inside the confinements are observed for a polarizable or non-polarizable surface treatment. Ionic liquid density profiles are slightly shifted toward the surface (about 0.1 Å) when surfaces are polarizable. This can be attributed to the mobile Drude charges in the first graphene layer, which orient themselves depending on the surrounding ions—shifting the center of mass slightly. While it was not possible to calculate the potential at zero charge (PZC) for the smaller confinements due to the absence of a bulk-like phase, it was estimated from Fig. S9 to be −0.23 V for the largest confinement.

However, the influence of the polarizable surfaces on the distribution of the individual ions is much more pronounced, as shown in Figs. 3(d) and 3(e). An increased layering, where the cation and anion are separated in more distinct areas, is observed for polarizable surfaces. The increase in the alternating arrangement is most pronounced in the first contact layer; in the case of the cation, the number density increases significantly—i.e., more than 20 nm⁻³ (~17.5%). The general layering for polarizable surfaces is illustrated in Fig. 4. While it is absent in the smaller pores, a stable bulk phase begins to form in the middle region of the third layer in the largest pore. However, before a stable bulk-like phase appears, the number density of the cation and anion alternate in the second (diffuse) layer caused by ion screening,⁷¹ while other peaks appear in the contact layers for both ions, which has been observed as well by Buraschi *et al.*⁴⁵ for another type of RTIL. Quite surprisingly, the smallest pore demonstrates no bulk or bulk-like phase and contact layers are divided by a diffuse-like zone alone [layer II in Fig. 4(c)]. This diffuse layer illustrates furthermore a rather unusual behavior as both ions show a maximum number density in this layer.

To investigate changes in the nearest neighborhood and molecular ordering in the different layers and confinement states, the cation–cation and cation–anion pair correlation functions (PCFs) are calculated layer-wise. Layer-wise pair correlation functions of all confinements with polarizable and non-polarizable surfaces can be

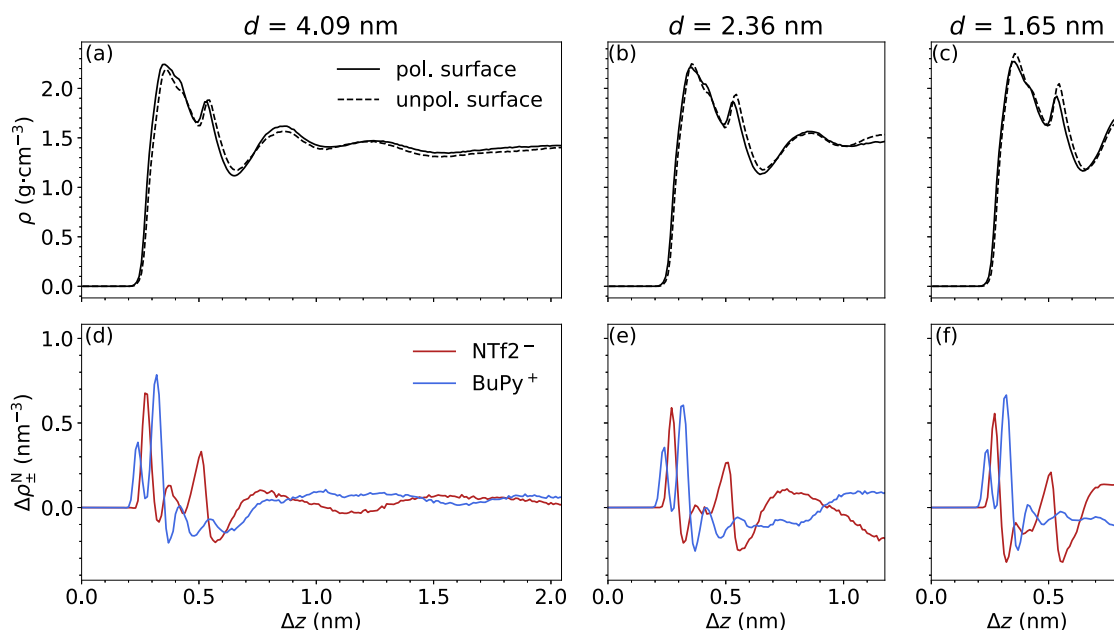


FIG. 3. Density profiles of the ionic liquid [BuPy][NTf2] in the three slit-pore confinements with a height of 4.09, 2.36, and 1.65 nm using polarizable (solid line) and non-polarizable (dotted line) surfaces (a)–(c). Ion density differences ($\Delta\rho_{\pm}^N = \rho_{\pm,\text{pol}}^N - \rho_{\pm,\text{unpol}}^N$) of BuPy⁺ (blue) and NTf2⁻ (red) between polarizable and non-polarizable surfaces are shown in panels (d)–(f), respectively. $\Delta z = 0$ coincides with the first layer of the graphite stack in contact with the RTIL.

found in Figs. S7 and S8, respectively. By using a cylindrical rather than the usual spherical integration volume, the calculated PCF only takes the neighboring molecules in the same layer into account. This approach makes it possible to investigate changes in the Coulombic ordering within each individual layer, as shown in Fig. 5, and is similar to the one from the work of Futamura *et al.*⁴³ While the contact layers in all three confinement heights have approximately the same structure, the composition in the diffuse layer of the narrowest confinement differs significantly from the others. As can be seen in the ratios of nearest neighbor ionic species in Fig. 5, the fraction of cations located in the first coordination shell of another cation increases significantly. Surprisingly, it is independent of the polarization of the surfaces (see the pie charts in Figs. S8 and S7 of the [supplementary material](#)). Due to a strong confinement, the ordering in particular layers is alternated in a way that the Coulombic ordering, in which an ion is mostly surrounded by ions of the opposite charge, is replaced by a block-wise alternating structure of same ion clusters. This so-called “superionic state” was first predicted for sub-nanometer pores by Kondrat and Kornyshev⁷² and later experimentally observed by Futamura *et al.*⁴³ However, the rearrangement associated with a superionic state was so far only observed in narrow confinements with a monolayer configuration and is associated with mirror charges induced on the surface, which decrease effectively Coulombic interactions between the ions.^{35,73,74} We observe that a similar change, albeit less dramatic, occurs already in the middle (diffuse) layer of the trilayer ionic liquid in the smallest confinement, which can be attributed to a pure confinement effect independent of the polarization of the surfaces. Hence, we call this specific situation a *quasi*-superionic state. For illustration, two

simulation snapshots of the respective contact and diffuse layers in the smallest confinement are shown in Fig. S6.

C. Ionic liquid dynamics in nanoconfinement

The influence of polarizable surfaces on the dynamics of the RTIL is investigated for all three confined states in the following. For both ion species, the diffusion coefficients are summarized in Table II. The diffusion coefficients with index I, II, or III (e.g., D_I^+) consider only the motion in the respective layers (cf. Fig. 4) and determine the diffusion according to the method described in Sec. II A. Overall diffusion coefficients D_{tot} correspond almost to the averaged diffusion of all cations or anions in each layer of the entire pore, respectively. Overall, the total diffusion is reduced for both ions in confinements, regardless of whether the surface is polarizable or not. The decrease becomes more pronounced as the slit-pore height continues to decrease. Apart from other differences in the total diffusion, it is quite remarkable that the increase in diffusion for both ions through a polarizable surface is about 80%–90% higher than for a non-polarizable surface for the smallest confinement. Moreover, a slower anion diffusion compared to the cation is observed for the largest confinement when the surface is polarizable. The surface polarization enhances the diffusivity of the specific ions studied here to a greater extent for smaller confinements.

To get a more detailed insight into the influence of the polarizable model on the confined dynamics—especially at the solid–liquid interface—the diffusion was calculated with respect to the layers shown in Fig. 4. The diffusion in the contact layer is always smaller than the total diffusion over the entire pore, as expected due to the

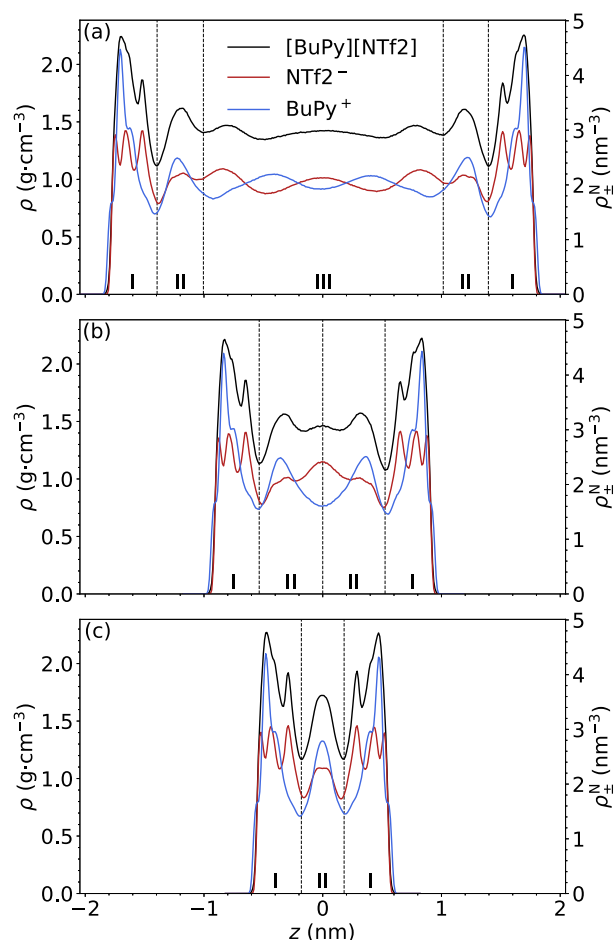


FIG. 4. Density profiles of a polarizable ionic liquid [BuPy][NTf2] in the three slit-pore confinements with polarizable surfaces and a height of (a) 4.09 nm, (b) 2.36 nm, and (c) 1.65 nm. The mass density of the ionic liquid is shown as a black line, while the blue and red lines represent the individual number densities ρ_{\pm}^N of BuPy⁺ and NTf2⁻, respectively.

stronger interaction and higher density in the contact layer and the consequent limitation of its mobility. For all three confinements, the diffusion increases toward the middle area of the pore for both ion species. It should be noted, however, that these layer-wise diffusion coefficients should be treated with caution, as the statistics for estimating an appropriate diffusion coefficient from the MSD can be quite poor. In addition, the aforementioned retention time would need to be increased to represent the time it may take for an ion to equilibrate in a new layer, but this is not possible due to the already quite extensive simulations. A more detailed discussion of this topic can be found in the [supplementary material](#).

D. Substrate dipole structure

Induced dipole moments in the surface layers are calculated according to Sec. II B for the whole system as well as for isolated ions adsorbed on the substrate (cf. Fig. S11 of the [supplementary](#)

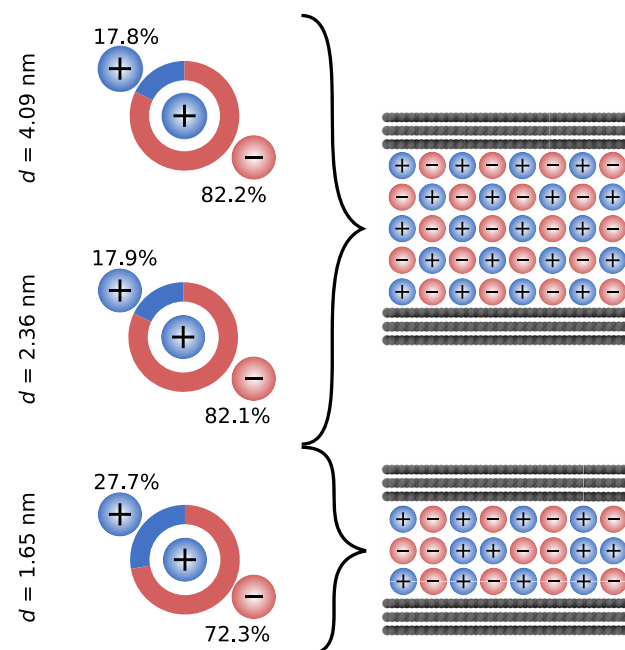


FIG. 5. Ratio of the BuPy⁺-BuPy⁺ (blue) and BuPy⁺-NTf2⁻ (red) coordination number in the diffuse layer (cf. layer II in Fig. 3) of all three confinements.

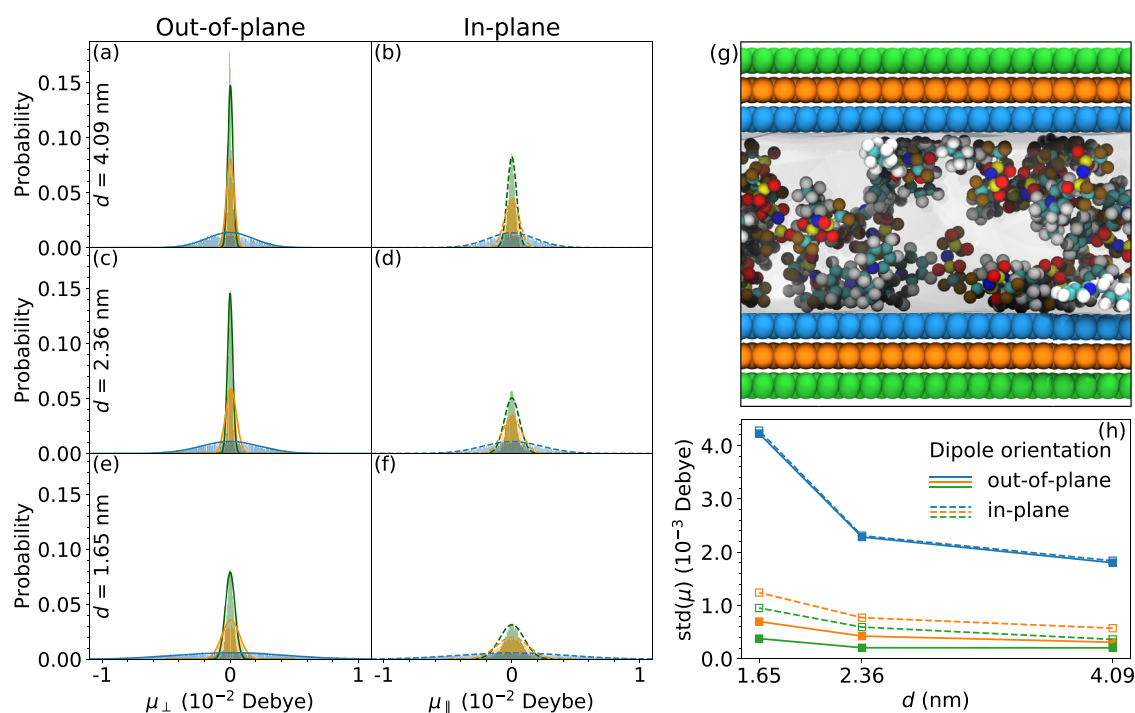
[material](#)). Moreover, induced dipoles are divided into two components: an out-of-plane and an in-plane dipole moment. In the case of isolated ions, the maximum induced dipole moments are about 0.10 D for both components. An isolated cation induces slightly smaller dipoles since it distributes its molecular charge over a wider range due to its larger size. However, it is remarkable that although out-of-plane and in-plane components have approximately the same maximum values in Fig. S11 of the [supplementary material](#), the in-plane polarization is much more far-reaching for both isolated ions.

Gaussians fitted to the dipole distributions of the liquid-filled pores shown in Fig. 6 can be used to determine an average surface dipole moment from the mean(μ), and the overall extent of the induced dipole moments in the respective substrate layer can be obtained from the standard deviation $\text{std}(\mu)$. Accompanying Gaussian fitting parameters are summarized in Table S5 of the [supplementary material](#). The distribution of induced dipoles shows that there is no pronounced net polarization of the surface in any particular direction, as might be anticipated given a more or less uniform charge distribution and an overall charge-neutral system. As expected, between the individual substrate layers, a strong reduction in the induced dipole moments is observed (cf. distribution widths in Fig. 6). However, this reduction is not equally distributed for both dipole orientations: While in the most inner graphene layer, the induced dipole moment is equally strong along both orientations, in the second and third layers, the in-plane polarization is more dominant than the out-of-plane polarization.

In general, a decrease in confinement height leads to an increase in induced dipole moments especially in the case of the smallest confinement. Most probably, the increase in induced dipole moments

TABLE II. Total and layer-wise diffusion coefficients of BuPy⁺ and NTf₂[−] in confinement with polarizable and non-polarizable surfaces. The layer-wise values are calculated according to the density profiles shown in Fig. 4.

d (nm)	D_{tot}^+	D_{tot}^-	D_{I}^+	D_{I}^-	D_{II}^+	D_{II}^-	D_{III}^+	D_{III}^-
Polarizable surface								
4.09	1.506	1.176	0.876	0.838	1.131	0.792	1.802	1.469
2.36	0.958	0.982	0.860	0.758	0.912	0.860	n/a	n/a
1.65	0.410	0.418	0.411	0.375	0.604	0.419	n/a	n/a
Non-polarizable surface								
4.09	1.584	1.499	0.842	0.952	1.344	0.816	1.898	1.888
2.36	0.725	0.702	0.673	0.629	0.851	0.639	n/a	n/a
1.65	0.215	0.215	0.201	0.214	0.283	0.244	n/a	n/a

**FIG. 6.** Distribution of the induced dipoles in each of the three substrate layers of all confinement heights divided into its out-of-plane [(a), (c), and (e)] and its in-plane component [(b), (d), and (f)]. Coloring of the distributions is according to the inset shown in (g). (h) $\text{std}(\mu)$ for each graphene layer decomposed in its out-of-plane (solid lines) and in-plane component (dashed lines).

is caused by the approaching of the two contact layers and hence a resulting higher charge density. For the reduction in the confinement height between 4.09 and 2.36 nm, the proportional change in the dipole moments in the two inner graphene layers is about the same; in the outermost layer, an increase in the more far-reaching in-plane polarization is observed while the out-of-plane dipole moment stays the same. By further reducing the confinement height (from 2.36 to 1.65 nm), the increase in the induced dipole moments is even more pronounced. The further enhancement of the induced dipoles

can be attributed to the reorientation of the ionic liquid in the diffuse layer, where the increasing aggregation of the same charged ions (cf. Fig. 5) creates larger charged clusters, which intensifies the effect of the mirror charges through the induced dipoles in the surface. Generally, the changes in the induced dipole moments follow the same pattern and magnitudes as the increase in the overall diffusion coefficient in Fig. 7 and illustrate a close relation between diffusion and induced dipoles in the surface—with an increasing impact on small confinements.

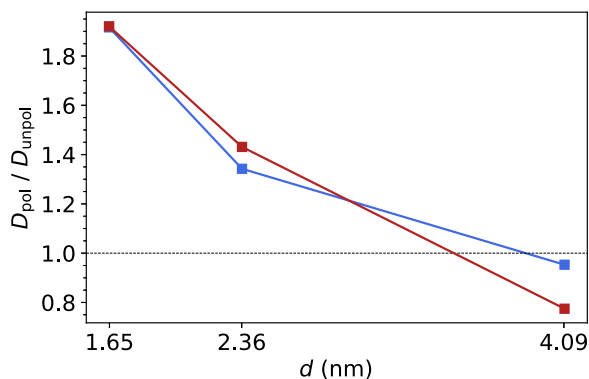


FIG. 7. Impact of a polarizable and non-polarizable surface on the diffusion D_{tot} of BuPy⁺ (blue) and NTf2⁻ (red).

IV. CONCLUSION

The influence of surface polarizability on confined RTILs in slit-like graphene pores was investigated using a parameterized, fully polarizable ionic liquid force field. The modified parameters for the RTIL [1-butylpyridinium (BuPy⁺) and bis(trifluoromethane)sulfonimide (NTf2⁻)] yield accurate overall densities and bulk dynamics in close agreement with recent experimentally determined values for the cation diffusion. Including the surface polarizability explicitly alters the density profiles of the cations and anions [cf. ρ_{\pm}^N in Figs. 3(d)–3(f)], although the overall density profile of the liquid remains almost unchanged [cf. Figs. 3(a)–3(c)], this change in the layering of the anions and cations upon inclusion of a polarizable surface model is associated with a dramatic increase in their diffusivity compared to non-polarizable surfaces. The contact layer shifts slightly closer to the surface that can be attributed to the reorientation of the dipoles according to the interacting ion and is consistent with previous studies of single ions on polarizable gold surfaces by Geada *et al.*⁴⁴ In the contact layer, the layer-like arrangement of the ions is enhanced by more than 15% due to the induced dipoles in the surface (cf. bottom panel of Fig. 3). Furthermore, a coalescence of the number density peaks of both ions (cf. Fig. 4) in the smallest confinement was observed, indicating an unusual ordering of the ions in the diffuse layer.

Aside from structural properties, a polarizable treatment of the surface impacts even more the dynamics of the RTIL in the confinement. In general, the explicit consideration of dipoles on the surfaces enhances the diffusion in the smallest and medium sized slit pores. An increase of up to nearly 100% was observed for cation diffusion in the smallest confinement compared to non-polarizable surfaces. Surprisingly, polarizable surfaces affect anion diffusion in the largest pore more than cation diffusion.

The analysis of individual ion diffusion in each layer shows that diffusion within the pores is highly variable and dependent on the confinement height. Due to the observed increased mobility of the ions (especially in the contact layer) in the case of a polarizable surface, one would intuitively assume that the explicit polarization of the surface would reduce the liquid–solid friction. However, this could not be validated within the error limits of additional simulations for friction (cf. Fig. S10 of the [supplementary material](#)).

Rather, the increased mobility can be attributed to the weakening of Coulomb forces between ions due to induced dipoles on the polarized surfaces—comparable to the increase in bulk mobility by polarizable models, which is the “result from attenuated long-range electrostatic interactions caused by enhanced screening from the polarization effect,” according to Yan *et al.*⁷⁵ The attenuation of Coulomb forces between ions by image charges on conducting and polarizable surfaces has already been observed for sub-nanometer confinements with a strong impact on the ionic liquid structure, i.e., a superionic state.^{18,43,74} Since here the confinement alone is responsible for the partial lifting of the Coulomb order in the central layer of the smallest confinement, independent of the surface polarization, we here refer to a *quasi*-superionic state. Interestingly, the Coulomb order is enhanced in the contact layer of all investigated pore sizes, and the first coordination shell of an ion consists almost exclusively of counterions, regardless of surface polarization. The strong Coulombic order is generally compensated by a less stringent Coulombic order in the next, the diffuse layer—except for the smallest pore, which considerably overcompensates it. Strong Coulomb order was also observed for pores containing a single molecular layer of an ionic liquid in the work of Futamura *et al.*,⁴³ indicating that the substrate is most likely responsible for the strong Coulomb order in the contact layer and the resulting overcompensation in the case of the smallest pore. However, it remains elusive why such an arrangement is favored in the contact layer and is an interesting point for further investigations.

Remarkably, the decrease in the diffusion occurs faster when the surface is non-polarizable (cf. Table II). The cation diffusion in the bulk-like region of the largest confinement is almost indistinguishable for polarizable and non-polarizable surfaces, while the anion diffusion is much slower compared to a non-polarizable surface. This behavior indicates a remarkable long-range impact of the surface polarization on the dynamics of the confined RTILs.

Comparing liquid-filled pores to isolated ions on the substrate, it has been observed that the induced dipole moments decrease by up to 90% in the surfaces due to the charge screening of the ions. Previous studies have often used isolated ions to estimate the number of polarizable substrate layers required. In contrast, our results suggest that polarization effects are much more attenuated for liquid-filled pores and, consequently, the number of required substrate layers could be effectively reduced. However, smaller confinements need a more careful consideration.

In addition to the newly proposed force field parameters for an accurate description of the here investigated RTIL, this study highlights the importance of accounting for the polarizability of both constituents in a solid–liquid interface when a strongly charged liquid is considered—which is in contrast to the findings of an uncharged polar liquid such as water in a previous study by Ho and Striolo.⁴² It is demonstrated that a polarizable treatment of the substrate surface is particularly important for small confinements and highly polar molecules, as often found in typical applications of ionic liquids at room temperature. Since the mobility of the ions has a significant impact on the dielectric constant and thus on the properties of ionic liquids in energy storage systems in general, the accurate description of the dynamics is a key factor for the evaluation of different RTILs in such systems. Although the isotropic Drude model already shows significant effects for this specific case investigated here, a more advanced anisotropic polarization model, particularly

for graphite substrates, would be desirable in order to investigate the importance of in-plane and out-of-plane polarization further.

SUPPLEMENTARY MATERIAL

The [supplementary material](#) contains simulation parameters, further details on MSD calculations, PCFs of the ionic liquid confined between polarizable and non-polarizable surfaces, simulation snapshots of the smallest confinement showing partial lifting of the Coulombic ordering, the electrostatic potential in the confinements, solid–liquid friction coefficients, and additional information on the induced dipoles in the surfaces.

ACKNOWLEDGMENTS

Helpful discussions with Jannes Seebeck and Tim Würger are gratefully acknowledged. This work was funded by the Deutsche Forschungsgemeinschaft (DFG, German Research Foundation)—Grant Nos. 390794421 and 192346071—GRK 2462 and SFB 986.

AUTHOR DECLARATIONS

Conflict of Interest

The authors have no conflicts to disclose.

DATA AVAILABILITY

The data that support the findings of this study are available from the corresponding author upon reasonable request.

REFERENCES

- 1 Y. U. Paulechka, D. H. Zaitsau, G. J. Kabo, and A. A. Strechan, *Thermochim. Acta* **439**, 158 (2005).
- 2 J. Zhao, X.-C. Jiang, C.-X. Li, and Z.-H. Wang, *Fluid Phase Equilib.* **247**, 190 (2006).
- 3 S. Zhang, N. Sun, X. He, X. Lu, and X. Zhang, *J. Phys. Chem. Ref. Data* **35**, 1475 (2006).
- 4 T.-Y. Wu, S.-G. Su, Y.-C. Lin, H. P. Wang, M.-W. Lin, S.-T. Gung, and I.-W. Sun, *Electrochim. Acta* **56**, 853 (2010).
- 5 C. P. Fredlake, J. M. Crosthwaite, D. G. Hert, S. N. V. K. Aki, and J. F. Brennecke, *J. Chem. Eng. Data* **49**, 954 (2004).
- 6 H.-P. Zhu, F. Yang, J. Tang, and M.-Y. He, *Green Chem.* **5**, 38 (2003).
- 7 S. Zhu, Y. Wu, Q. Chen, Z. Yu, C. Wang, S. Jin, Y. Ding, and G. Wu, *Green Chem.* **8**, 325 (2006).
- 8 S. Ding, M. Radosz, and Y. Shen, *Macromolecules* **38**, 5921 (2005).
- 9 C. Dai, J. Zhang, C. Huang, and Z. Lei, *Chem. Rev.* **117**, 6929 (2017).
- 10 J. Sun, W. Cheng, W. Fan, Y. Wang, Z. Meng, and S. Zhang, *Catal. Today* **148**, 361 (2009).
- 11 O. Aaltonen and O. Jauhiainen, *Carbohydr. Polym.* **75**, 125 (2009).
- 12 G. R. Zhang and B. J. M. Etzold, *Adv. Funct. Mater.* **31**, 2010977 (2021).
- 13 A. Balducci, U. Bardi, S. Caporali, M. Mastragostino, and F. Soavi, *Electrochem. Commun.* **6**, 566 (2004).
- 14 A. Brandt, S. Pohlmann, A. Varzi, A. Balducci, and S. Passerini, *MRS Bull.* **38**, 554 (2013).
- 15 A. Lewandowski, A. Olejniczak, M. Galinski, and I. Stepniak, *J. Power Sources* **195**, 5814 (2010).
- 16 E. Frackowiak, G. Lota, and J. Pernak, *Appl. Phys. Lett.* **86**, 164104 (2005).
- 17 C. Péan, C. Merlet, B. Rotenberg, P. A. Madden, P.-L. Taberna, B. Daffos, M. Salanne, and P. Simon, *ACS Nano* **8**, 1576 (2014).
- 18 S. Kondrat, P. Wu, R. Qiao, and A. A. Kornyshev, *Nat. Mater.* **13**, 387 (2014).
- 19 Y. He, R. Qiao, J. Vatamanu, O. Borodin, D. Bedrov, J. Huang, and B. G. Sumpter, *J. Phys. Chem. Lett.* **7**, 36 (2015).
- 20 H. Ohno, *Reference Module in Chemistry, Molecular Sciences and Chemical Engineering* (Elsevier, 2013).
- 21 M. A. Navarra, *MRS Bull.* **38**, 548 (2013).
- 22 K. Liu, Z. Wang, L. Shi, S. Jungsuttiwong, and S. Yuan, *J. Energy Chem.* **59**, 320 (2021).
- 23 J. P. C. Trigueiro, R. L. Lavall, and G. G. Silva, *J. Power Sources* **256**, 264 (2014).
- 24 Y. Tan, C. Xu, G. Chen, N. Zheng, and Q. Xie, *Energy Environ. Sci.* **5**, 6923 (2012).
- 25 D. Nuvoli, L. Valentini, V. Alzari, S. Scognamiglio, S. B. Bon, M. Piccinini, J. Illescas, and A. Mariani, *J. Mater. Chem.* **21**, 3428 (2011).
- 26 J. Seebeck, P. Schifffels, S. Schweizer, J.-R. Hill, and R. H. Meißner, *J. Phys. Chem. C* **124**, 5515 (2020).
- 27 N. N. Rajput, J. Monk, and F. R. Hung, *J. Phys. Chem. C* **118**, 1540 (2014).
- 28 C. Merlet, B. Rotenberg, P. A. Madden, P.-L. Taberna, P. Simon, Y. Gogotsi, and M. Salanne, *Nat. Mater.* **11**, 306 (2012).
- 29 C. Merlet, M. Salanne, and B. Rotenberg, *J. Phys. Chem. C* **116**, 7687 (2012).
- 30 Z. Yan, D. Meng, X. Wu, X. Zhang, W. Liu, and K. He, *J. Phys. Chem. C* **119**, 19244 (2015).
- 31 C. Noh and Y. Jung, *Phys. Chem. Chem. Phys.* **21**, 6790 (2019).
- 32 S. Tsuzuki, W. Shinoda, H. Saito, M. Mikami, H. Tokuda, and M. Watanabe, *J. Phys. Chem. B* **113**, 10641 (2009).
- 33 C. Cadena, Q. Zhao, R. Q. Snurr, and E. J. Maginn, *J. Phys. Chem. B* **110**, 2821 (2006).
- 34 D. Bedrov, J.-P. Piquemal, O. Borodin, A. D. MacKerell, B. Roux, and C. Schröder, *Chem. Rev.* **119**, 7940 (2019).
- 35 K. Breitsprecher, C. Holm, and S. Kondrat, *ACS Nano* **12**, 9733 (2018).
- 36 E. Choi, J. G. McDaniel, J. R. Schmidt, and A. Yethiraj, *J. Phys. Chem. Lett.* **5**, 2670 (2014).
- 37 J. G. McDaniel and A. Yethiraj, *J. Phys. Chem. Lett.* **9**, 4765 (2018).
- 38 T. Yan, C. J. Burnham, M. G. Del Pópolo, and G. A. Voth, *J. Phys. Chem. B* **108**, 11877 (2004).
- 39 A. d. O. Cavalcante, M. C. C. Ribeiro, and M. S. Skaf, *J. Chem. Phys.* **140**, 144108 (2014).
- 40 K. Goloviznina, J. N. Canongia Lopes, M. Costa Gomes, and A. A. H. Pádua, *J. Chem. Theory Comput.* **15**, 5858 (2019).
- 41 J. B. Haskins and J. W. Lawson, *J. Chem. Phys.* **144**, 184707 (2016).
- 42 T. A. Ho and A. Striolo, *J. Chem. Phys.* **138**, 054117 (2013).
- 43 R. Futamura, T. Iiyama, Y. Takasaki, Y. Gogotsi, M. J. Biggs, M. Salanne, J. Ségalini, P. Simon, and K. Kaneko, *Nat. Mater.* **16**, 1225 (2017).
- 44 I. L. Geada, H. Ramezani-Dakhel, T. Jamil, M. Sulpizi, and H. Heinz, *Nat. Commun.* **9**, 716 (2018).
- 45 M. Buraschi, S. Sansotta, and D. Zahn, *J. Phys. Chem. C* **124**, 2002 (2020).
- 46 M. Busch, T. Hofmann, B. Frick, J. P. Embs, B. Dyatkin, and P. Huber, *Phys. Rev. Mater.* **4**, 055401 (2020).
- 47 S. Plimpton, *J. Comput. Phys.* **117**, 1 (1995).
- 48 G. Lamoureux and B. Roux, *J. Chem. Phys.* **119**, 3025 (2003).
- 49 W. Humphrey, A. Dalke, and K. Schulten, *J. Mol. Graphics* **14**, 33 (1996).
- 50 A. Padua, agiliopadua/fftool, <https://github.com/padua-group/fftool>, 2019.
- 51 L. Martínez, R. Andrade, E. G. Birgin, and J. M. Martínez, *J. Comput. Chem.* **30**, 2157 (2009).
- 52 J. N. Canongia Lopes and A. A. H. Pádua, *J. Phys. Chem. B* **110**, 19586 (2006).
- 53 A. Dequidt, J. Devémy, and A. A. H. Pádua, *J. Chem. Inf. Model.* **56**, 260 (2016).
- 54 A. A. H. Pádua, *J. Chem. Phys.* **146**, 204501 (2017).
- 55 B. T. Thole, *Chem. Phys.* **59**, 341 (1981).
- 56 E. Heid, A. Szabadi, and C. Schröder, “Quantum mechanical determination of atomic polarizabilities of ionic liquids,” *Phys. Chem. Chem. Phys.*, **20**, 10992–10996 (2018).
- 57 S. Ntim and M. Sulpizi, *Phys. Chem. Chem. Phys.* **22**, 10786 (2020).
- 58 L. Scalfi, D. T. Limmer, A. Coretti, S. Bonella, P. A. Madden, M. Salanne, and B. Rotenberg, *Phys. Chem. Chem. Phys.* **22**, 10480 (2020).

- ⁵⁹L. J. V. Ahrens-Iwers and R. H. Meißner, *J. Chem. Phys.* **155**, 104104 (2021).
- ⁶⁰A. Marin-Laflèche, M. Haefele, L. Scalfi, A. Coretti, T. Dufils, G. Jeanmairet, S. Reed, A. Serva, R. Berthin, C. Bacon, S. Bonella, B. Rotenberg, P. Madden, and M. Salanne, *J. Open Source Software* **5**, 2373 (2020).
- ⁶¹K. Breitsprecher, K. Szuttor, and C. Holm, *J. Phys. Chem. C* **119**, 22445 (2015).
- ⁶²E. K. Yu, D. A. Stewart, and S. Tiwari, *Phys. Rev. B* **77**, 195406 (2008).
- ⁶³R. P. Misra and D. Blankschtein, *J. Phys. Chem. C* **121**, 28166 (2017).
- ⁶⁴I.-C. Yeh and M. L. Berkowitz, *J. Chem. Phys.* **111**, 3155 (1999).
- ⁶⁵J. Rafiee, X. Mi, H. Gullapalli, A. V. Thomas, F. Yavari, Y. Shi, P. M. Ajayan, and N. A. Koratkar, *Nat. Mater.* **11**, 217 (2012).
- ⁶⁶S. V. Sambasivarao and O. Acevedo, *J. Chem. Theory Comput.* **5**, 1038 (2009).
- ⁶⁷M. J. Robertson, J. Tirado-Rives, and W. L. Jorgensen, *J. Chem. Theory Comput.* **11**, 3499 (2015).
- ⁶⁸P. E. M. Lopes, B. Roux, and A. D. MacKerell, *Theor. Chem. Acc.* **124**, 11 (2009).
- ⁶⁹V. Ballenegger, A. Arnold, and J. J. Cerdà, *J. Chem. Phys.* **131**, 094107 (2009).
- ⁷⁰J. P. Embs, T. Burankova, E. Reichert, and R. Hempelmann, *J. Phys. Chem. B* **116**, 13265 (2012).
- ⁷¹C. Merlet, D. T. Limmer, M. Salanne, R. van Roij, P. A. Madden, D. Chandler, and B. Rotenberg, *J. Phys. Chem. C* **118**, 18291 (2014).
- ⁷²S. Kondrat and A. Kornyshev, *J. Phys.: Condens. Matter* **23**, 022201 (2010).
- ⁷³M. Dudka, S. Kondrat, A. Kornyshev, and G. Oshanin, *J. Phys.: Condens. Matter* **28**, 464007 (2016).
- ⁷⁴S. Kondrat, N. Georgi, M. V. Fedorov, and A. A. Kornyshev, *Phys. Chem. Chem. Phys.* **13**, 11359 (2011).
- ⁷⁵T. Yan, Y. Wang, and C. Knox, *J. Phys. Chem. B* **114**, 6886 (2010).